Overview on numerical studies of reconnection and dissipation in the solar wind

S. Donato, S. Servidio, P. Dmitruk, F. Valentini, A. Greco, P. Veltri, M. Wan, M. A. Shay, P. A. Cassak, and W. H. Matthaeus

Citation: AIP Conference Proceedings **1539**, 99 (2013); doi: 10.1063/1.4810999
View online: https://doi.org/10.1063/1.4810999
View Table of Contents: http://aip.scitation.org/toc/apc/1539/1
Published by the American Institute of Physics

Overview on numerical studies of reconnection and dissipation in the solar wind

S. Donato*, S. Servidio*, P. Dmitruk†, F. Valentini*, A. Greco*, P. Veltri*, M. Wan**, M.A. Shay**, P.A. Cassak‡ and W.H. Matthaeus**

*Dipartimento di Fisica, Università della Calabria, I-87036 Cosenza, Italy
†Departmento de Física, Facultad de Ciencias Exactas y Naturales, Universidad de Buenos Aires, and IFIBA, CONICET, Ciudad Universitaria, 1428, Buenos Aires, Argentina
**Bartol Research Institute and Department of Physics and Astronomy, University of Delaware, Newark, DE 19716, USA
‡Department of Physics, West Virginia University, Morgantown, WV 26506, USA

Abstract. In this work, recent advances in numerical studies of local reconnection events in the turbulent plasmas are reviewed. Recently [1], the nonlinear dynamics of magnetic reconnection in turbulence has been investigated through high resolution numerical simulations. Both fluid (MHD and Hall MHD) and kinetic (HybridVlasov) 2D simulations reveal the presence of a large number of X-type neutral points, where magnetic reconnection locally occurs. The associated reconnection rates are distributed over a wide range of values and they depend on the local geometry of the diffusion region. This new approach to the study of magnetic reconnection has broad applications to the turbulent solar wind (SW). Strong magnetic SW discontinuities are in fact strongly related to these intermittent processes of reconnection [2, 3]. Methods employed to identify sets of possible reconnection events along a one-dimensional path through the turbulent field (emulating experimental sampling by a single detector in a highspeed flow) are here reviewed. These local reconnection/discontinuity events may be the main sites of heating and particle acceleration processes [4]. Results from hybrid-Vlasov kinetic simulations support these observations [5, 6]. In the turbulent regime, in fact, kinetic effects manifest through a deformation of the ion distribution function. These patterns of non-Maxwellian features are concentrated in space nearby regions of strong magnetic activity. These results open a new path on the study of kinetic processes such as heating, particle acceleration, and temperature anisotropy, commonly observed in astrophysics.

Keywords: Magnetic Reconnection, Plasma simulations, Plasma Turbulence, Solar Wind
PACS: 52.35.Ra, 52.35.Vd, 52.65.-y, 96.50.Bh, 96.60.Iv, 96.60.Vg

INTRODUCTION

Magnetic reconnection is a fundamental phenomenon in magnetized plasmas, responsible for magnetic energy release, topology change and particle energization, and therefore it is of widespread relevance in astrophysical and laboratory systems [7, 8, 9]. Another underlying common feature of the above systems is the presence of turbulence [10], so a simultaneous description of both reconnection and turbulence is needed. Recently [1, 11], it has been proposed that turbulence provides a kind of unbiased and natural local boundary condition for reconnection, producing much faster reconnection events than one would expect in laminar regimes. In those works, direct numerical simulations of decaying incompressible two-dimensional magnetohydrodynamics (MHD) reveal that in fully developed turbulence complex processes of reconnection locally occur. The complex scenario consists of multiple-reconnection simultaneous events involving different-size magnetic vortices.

Besides turbulence [12], another ingredient that may accelerate the process of reconnection is the Hall effect [13]. The latter is always important for dynamical processes that occur at scales comparable to the ion skin depth, defined as $d_i = c/\omega_{pi}$ (ω_{pi} being the ion plasma frequency). The Hall effect become globally important and even dominant as the ion skin depth becomes comparable to the system size L_0, namely when $d_i/L_0 \neq 0$ [14]. Generally, the Hall effect is thought to be fundamental for astrophysical plasmas, since it modifies small scale turbulent activity, producing a departure from MHD predictions [15, 16, 17]. A study on the comparison between MHD and Hall MHD, through high resolution pseudo-spectral numerical simulations, reveals that an increase of the Hall parameter broadens the distribution of reconnection rates and changes the local geometry of the reconnection region, leading locally to faster reconnection processes [18].

The preferential sites for small-scale turbulent reconnection are very thin current sheets [19], that represent a fraction of the most common solar wind discontinuities. Starting from this new approach we put a link between solar wind discontinuities and local magnetic reconnection processes. Solar wind discontinuities are

Solar Wind 13
AIP Conf. Proc. 1539, 99-104 (2013); doi: 10.1063/1.4810999

characterized by large and rapid changes in properties of the plasma and magnetic field [20, 21]. Recent studies on magnetic discontinuities show that their statistical properties are very similar to distributions obtained from simulations of MHD turbulence [2, 3]. This line of reasoning argues that thin current sheets are characteristic coherent structures expected in active intermittent MHD turbulence [22], and which are therefore integral to the dynamical couplings across scales. Therefore, solar wind discontinuities are one of the best applications of our theory of reconnection-in-turbulence. Here, using MHD simulations, we review that methods for identifying intermittent current sheet-like structures can identify sets of structures that are likely to be active reconnection regions. Applications to the study of solar wind discontinuities are reviewed, comparing simulations to spacecraft observations.

In turbulence, coherent structures are expected to be sites of enhanced inhomogeneous dissipation. Such small scale dissipative structures, through kinetic processes, may be candidates to be active sites of magnetic reconnection, heating and temperature anisotropy [23, 24, 25]. To support this idea, kinetic processes are investigated in a two-dimensional turbulent plasma using direct numerical simulations of a hybrid Vlasov-Maxwell model. In the turbulent regime, kinetic effects manifest through a deformation of the ion distribution function. The analysis shows that the distribution function is strongly modulated by the electromagnetic field, and elongates mainly or across the local magnetic field [5]. These departures from a Maxwellian equilibrium may be responsible for the production of heating and anisotropy, commonly observed in many astrophysical and laboratory systems.

MAGNETIC RECONNECTION IN 2D MHD TURBULENCE

The 2D incompressible MHD equations can be written in terms of the magnetic potential $a(x,y)$ and the stream function $\psi(x,y)$. By choosing a uniform mass density $\rho = 1$, the equations read [26]:

$$\frac{\partial \omega}{\partial t} = -(\boldsymbol{v}\cdot\boldsymbol{\nabla})\,\omega + (\boldsymbol{b}\cdot\boldsymbol{\nabla})\,j + R_v^{-1}\boldsymbol{\nabla}^2\omega, \qquad (1)$$

$$\frac{\partial a}{\partial t} = -(\boldsymbol{v}\cdot\boldsymbol{\nabla})\,a + R_\mu^{-1}\boldsymbol{\nabla}^2 a, \qquad (2)$$

where the magnetic field is $\boldsymbol{b} = \boldsymbol{\nabla}a \times \hat{\boldsymbol{z}}$, the velocity $\boldsymbol{v} = \boldsymbol{\nabla}\psi \times \hat{\boldsymbol{z}}$, the current density $j = -\boldsymbol{\nabla}^2 a$, and the vorticity $\omega = -\boldsymbol{\nabla}^2\psi$. Eqs. (1)-(2) are written in Alfvén units [27] with lengths scaled to L_0. The latter is a typical large scale length such that the box size is set to $2\pi L_0$. Velocities and magnetic fields are normalized to the root mean square Alfvén speed V_A and time is scaled to L_0/V_A. R_μ and R_v are the magnetic and kinetic Reynolds numbers, respectively (at scale L_0). Eqs. (1)-(2) are solved in a

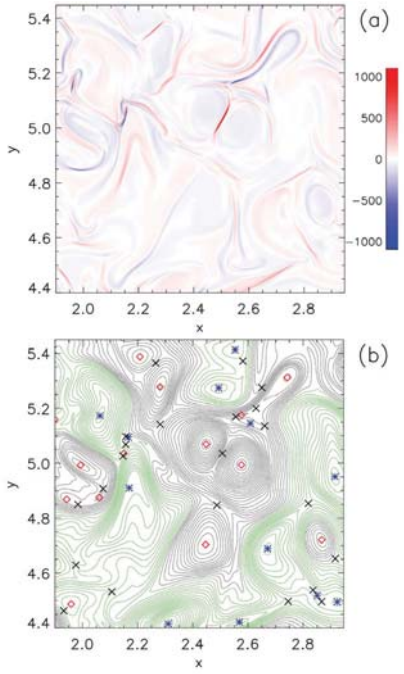

FIGURE 1. (a) Shaded-contour plot of the current density j. (b) Line-contour of the magnetic potential a with the position of all the critical points: O-points (blue stars for the maxima and red open-diamonds for the minima) and X-points (black $\times$). From a run with 8192^2 grid points.

periodic Cartesian geometry (x,y), using a well tested dealiased (2/3 rule) pseudo-spectral code [28] with resolutions from 4096^2 up to 16384^2 reaching Reynolds numbers $R_v = R_\mu \sim 10000$ (more details can be found in [29]).

For the statistical analysis we considered the state of the system at which the mean square current density $\langle j^2 \rangle$ is very near to its peak value. At this instant of time the peak of small scale turbulent activity is achieved, and coherent structures appear. They can be identified as magnetic islands (or vortices). The current density j becomes very high in narrow layers between islands (Fig. 1-(a)). These coherent structures interact non-linearly, merge, stretch, connect, attract and repel each other. Reconnection is a major element of this complex interaction.

In order to describe the local processes of reconnection that spontaneously develop in turbulence we examine the topology of the magnetic potential studying the *H*essian matrix of a, defined as

$$H^a_{i,j}(\boldsymbol{x}) = \frac{\partial^2 a}{\partial x_i \partial x_j}, \qquad (3)$$

which we evaluate at the neutral points of the magnetic field. At each neutral point, where $\nabla a = 0$, we compute the eigenvalues of $H_{i,j}$. If both eigenvalues are positive (negative), the point is a local minimum (maximum) of a (an O point). If the eigenvalues are of mixed sign, it is a saddle point (an X point). Further details on the methodology are provided in [11]. In Fig. 1-(b) an example of a magnetic potential landscape together with its critical points are reported for a subregion of the simulation box. The local geometry of the diffusion region is related to the Hessian eigenvalues, $\lambda_1 = \frac{\partial^2 a}{\partial s^2}$ and $\lambda_2 = \frac{\partial^2 a}{\partial l^2}$, the larger and smaller (in magnitude), respectevely. The coordinate s is associated with the minimum thickness δ of the current sheet, while l with the elongation ℓ. From a scaling analysis, the aspect ratio of the diffusion region is well approximated by

$$\ell/\delta \simeq \sqrt{|\lambda_1/\lambda_2|}. \quad (4)$$

Once the position of all critical point is obtained it is possible to find the reconnection rate of two island, through $\partial a/\partial t$ and it is equal to the electic field measured at the X-point ($\partial a/\partial t = -E_\times = (R_\mu^{-1} j)_\times$). These rates are then normalized to the mean square fluctuation δb^2_{rms}, appropriate for Alfvènic turbulence. Fig. 2-(a) shows that the reconnection rates are broadly distributed with a range $|E_\times| \in [10^{-6}, 0.3]$ with $\langle |E_\times| \rangle \simeq 0.05$. The distribution of reconnection rates PDF($|E_\times|$), for a run with 4096^2 grid points, is reported in Fig. 3-(a) (red curve) and it is broad and peaked around zero value. In the case in which the reconnection is in a stationary state, the rate depends on the aspect ratio defined by Eq. (4). From Fig. 2-(a) it should be noted that the strongest reconnection rate scale as $E_\times \sim \ell/\delta \sim \sqrt{\lambda_R}$, where $\lambda_R = \left|\frac{\lambda_1}{\lambda_2}\right|$. These fastest reconnection events in MHD turbulence can be described by a modified Sweet-Parker theory which takes into account asymmetries (consequence of the asymmetric nature of turbulent reconnection) in the reconnecting magnetic field [30]. This model predicts that the reconnection rate scales as

$$E_\times^{th} = \sqrt{\frac{b_1^{3/2} b_2^{3/2}}{R_\mu \ell}} \quad (5)$$

where b_1 and b_2 are the upstream magnetic fields on each side of the X-point. Fig. 2-(b) shows that in all the simulations the reconnection rates are consistent with the prediction given by Eq. (5)

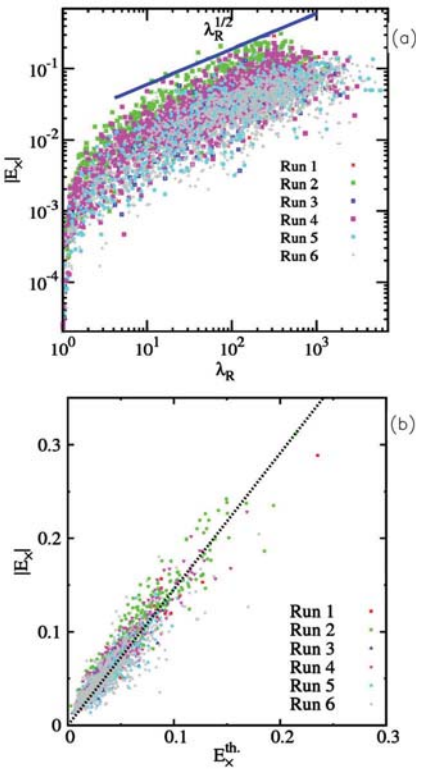

FIGURE 2. (a) Scatter plot of the reconnection rates *vs.* the geometry of the reconnection region (ratio of the eigenvalues λ_R). The presence of a power-law fit (blue line) demonstrates that there is a relation between the reconnection rate and the geometry of the diffusion region. (b) Computed reconnection rates *vs.* expectation from Eq. (5) [30]. The good agreement indicates that the system is reconnecting in a asymmetric Sweet-Parker scenario. Resolution runs from 4096^2 up to 16384^2 (see [11] for more details).

MHD VS. HALL MHD

Analogously to MHD, the equations of incompressible Hall MHD can be written in dimensionless form. In 2.5D (2 dimensions in the physical space for three-dimensional components) the equations read:

$$\frac{\partial \boldsymbol{v}}{\partial t} = -(\boldsymbol{v}\cdot\nabla)\boldsymbol{v} - \nabla P + \boldsymbol{j}\times\boldsymbol{b} + R_\nu^{-1}\nabla^2\boldsymbol{v}, \quad (6)$$

$$\frac{\partial \boldsymbol{b}}{\partial t} = \nabla\times[(\boldsymbol{v} - \varepsilon_H \boldsymbol{j})\times\boldsymbol{b}] + R_\mu^{-1}\nabla^2\boldsymbol{b}. \quad (7)$$

The fields can be decomposed in perpendicular (in-plane) and parallel (out-of-plane, along z) components, namely $\boldsymbol{b} = (\boldsymbol{b}_\perp, b_z)$ and $\boldsymbol{v} = (\boldsymbol{v}_\perp, v_z)$. For the magnetic field $\boldsymbol{b}_\perp = \nabla a \times \hat{z}$, where a is the magnetic potential. The coefficient $\varepsilon_H = d_i/L_0$ is the Hall parameter and is proportional to the amount of dispersive effects present in the system. Note that, for $\varepsilon_H \to 0$, Eqs. (6)-(7) reduce to MHD [see Eqs. (1) - (2)]. The above equations are

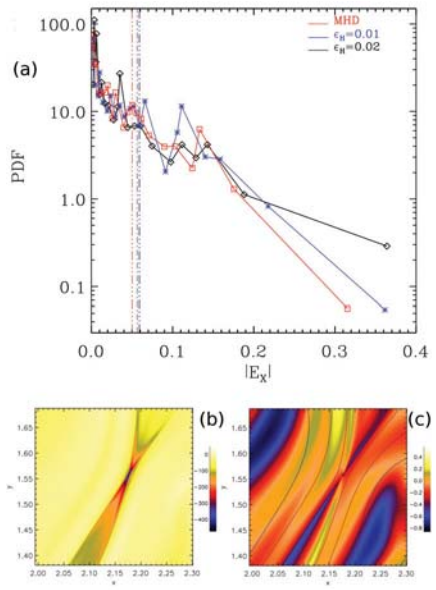

FIGURE 3. (a) PDF of the reconnection rates for $\varepsilon_H = 0$ (MHD, red squares), $\varepsilon_H = 1/100$ (blue stars) and $\varepsilon_H = 1/50$ (black rhombus). The vertical dash-dotted lines represent the mean value of each distribution $\langle |E_\times| \rangle$. (b)-(c) Respectevely, a contour plot of the out-of-plane components of current j_z and of the magnetic field b_z in a sub-region of the simulation box. The bifurcation of the sheet and a quadrupole structure in the magnetic field can be identified.

solved with the same algorithm used for the MHD case, using 4096^2 grid points, and with $R_\mu = R_\nu = 1700$ with different values for the coefficient ε_H. The detailed discussion about results on reconnection in Hall MHD turbulence has been recently published in [18]). In this publication it was showed that an increase of weight of the Hall parameters reflects in a higher small scale activity that is responsible for increasing intermittency in the system, and is generally attributed to the presence of dispersive effects [31]. The PDF of $E_\times$ (constructed using constant weight m per-bin [10]), for MHD and Hall MHD cases, are reported in Fig. 3(a). As expected, both distributions manifest strong departures from the averages. In the HMHD cases higher tails appear in the PDF indicates that the Hall term slightly accelerates reconnection. This analysis confirms that when the Hall physics is present, distributions of reconnection rates become broader than the MHD case, leading to slightly faster rates on average, but revealing more frequently occurring explosive (very large) reconnection events than in the MHD case.

To capture the influence of the Hall physics, one should look at the local structure of the current. The introduction of the Hall effect affects the local geometry of the reconnection regions, producing a clear bifurcations in the current sheets (Fig. 3-(b)) and, as expected from theory [13], a quadrupolar structure of the magnetic field (Fig. 3-(c)). The magnetic field shows four distinctive polarities, organized with respect to the X-point, a clear signature of Hall effect in turbulent reconnection. Another interesting feature (not shown) is that the HMHD current sheets are shorter and thinner. This is reminiscent of the systematic shortening and thinning of current sheets seen in isolated laminar reconnection simulations [32].

INTERMITTENT STRUCTURES AND RECONNECTION IN MHD TURBULENCE

Here, using simulations of 2D MHD turbulence, we explore a possible link between tangential discontinuities and magnetic reconnection. The goal is to develop nemerical algorithms that may be useful for solar wind applications. Following [33], rapid changes in the magnetic field are described looking at the increments $\Delta\mathbf{b}(s,\Delta s) = \mathbf{b}(s+\Delta s) - \mathbf{b}(s)$, calculated along a 1D path s in the simulation box, which emulates the spacecraft measurements, on a spatial separation or lag Δs. Employing only the sequence of magnetic increments, we computed the normalized magnitude

$$\Im(\Delta s, \ell, s) = \frac{|\Delta\mathbf{b}(s,\Delta s)|}{\sqrt{\langle |\Delta \boldsymbol{b}(s,\Delta s)|^2 \rangle_\ell}}, \qquad (8)$$

where $\langle \bullet \rangle_\ell = (1/\ell) \int_\ell \bullet ds$ denotes a spatial average over an interval of length ℓ, and Δs is the spatial lag of the increment). The square of the above quantity has been called the *Partial Variance of Increments* (PVI) [2].

For the numerical analysis performed $\ell \simeq 535\lambda_C$, where $\lambda_C = 0.18$ is the turbulence correlation length - a natural scale for computing averages. The PVI time series, evaluated using Eqs. (8) is reported in Fig. 4-(a). The illustration spans more than 500 correlation lengths. This spatial signal has been compared to a time signal measured by a ACE solar wind spacecraft, near 1 AU, over a period of about 20 days (panel (b)), where the time signal is converted to a spatial signal, using the average velocity of the flow (details in [33]).

The PVI increment time series is bursty, suggesting the presence of sharp gradients and localized coherent structures in the magnetic field, that represent the spatial intermittency of turbulence. These events may correspond to what are qualitatively called "tangential discontinuities" (TD) and, possibly, to reconnection events. Examples of TD selected by the PVI method are displayed in Fig. 4, in simulation data (panel (c)) and in solar wind data [3] (panel (d)). Imposing a threshold θ on Eq. (8), a collection of stronger discontinuities along the path s can be identified. That is, we selected portions of the trajectory

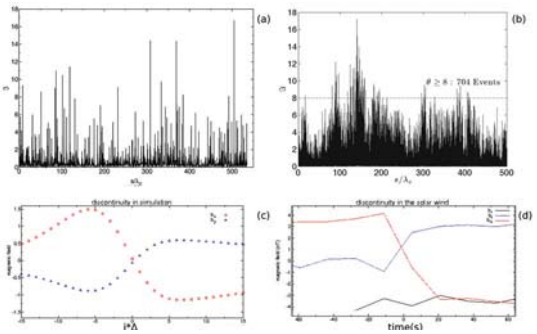

FIGURE 4. (a) Spatial signal $\Im(\Delta s, \ell, s)$ (PVI) obtained from the simulation by sampling along the trajectory s in the simulation box. (b) Same quantity obtained from solar wind data. (c) The two components of the magnetic field vector in simulation data. (d) The three components of the magnetic field vector in solar wind data in the RTN reference frame

in which the condition $\Im(\Delta s, \ell, s) > \theta$ is satisfied, and we employed this condition to identify candidate reconnection sites (these regions are determined using a map generated by the cellular automaton procedure described in [11]). For high θ, all the TDs correspond to reconnection sites. In general, we suggest that the methods developed here may have many applications to the the solar wind data, where the coexistence of turbulence and magnetic reconnection cannot be discarded.

RECONNECTION IN VLASOV TURBULENCE

Here, using a Eulerian algorithm [34, 35] in a 2D-3V geometry (two dimensions in physical space and three in velocity space), we present a statistical description of the link between the magnetic skeleton of turbulence and the velocity subspace of the distribution function (DF). The goal was to investigate the link between spatial magnetic structures, such as magnetic vortices, and the formation of non-Maxwellian features. Results have been published on [5].

The dimensionless hybrid Vlasov-Maxwell equations (kinetic ions and fluid electrons) are given by [34, 35]

$$\partial_t f + \boldsymbol{\nabla}\cdot(\boldsymbol{v}f) + \boldsymbol{\nabla}_{\boldsymbol{v}}\cdot[(\boldsymbol{E}+\boldsymbol{v}\times\boldsymbol{B})f] = 0 \qquad (9)$$
$$\partial_t \boldsymbol{B} = -\boldsymbol{\nabla}\times\boldsymbol{E},\ \ \boldsymbol{E} = -\boldsymbol{u}\times\boldsymbol{B} + \boldsymbol{j}\times\boldsymbol{B}/n - \boldsymbol{\nabla}P_e/n + \eta\boldsymbol{j}$$

where $f(\boldsymbol{x},\boldsymbol{v}) \equiv f(x,y,v_x,v_y,v_z)$ is the ion DF, $\boldsymbol{E}$ the electric field, $\boldsymbol{B} = \boldsymbol{b} + \boldsymbol{B}_0$ the total magnetic field ($\boldsymbol{B}_0 = B_0\hat{z}$ is the mean field), and $\boldsymbol{j} = \boldsymbol{\nabla}\times\boldsymbol{b}$ the total current density. The ion density n and the ion bulk velocity $\boldsymbol{u}$ are obtained as the velocity moments of f, while an isothermal equation of state for the electron pressure P_e has been assigned. Times are scaled by the cyclotron time Ω_{ci}^{-1}, velocities by the Alfvén speed V_A, lengths by the ion skin depth $d_i = V_A/\Omega_{ci}$, and masses by the ion mass m_i. Runs were performed with 512^2 mesh points in physical space and 51^3 in velocity space. To investigate the influence of both turbulence and system size, we performed different runs varying $\delta b/B_0$ ($\delta b = \langle b_x^2 + b_y^2)\rangle$ and $\langle\bullet\rangle$ represents spatial averages) and L_0/d_i (being L_0 the system size). More details about numerical methods, accuracy and initial conditions in [5].

In analogy with fluid models, the analysis has been done at the time τ at which the turbulent activity is maximum. This time is estimated measuring the average out-of-plane squared current density $\langle j_z^2\rangle$. At this time of simulation, as seen in MHD and Hall MHD models, turbulence manifests through the appearance of coherent structures, exhibiting a sea of vortices and current sheets. In between islands the out-of-plane component of the current (j_z) becomes very intense, and in these regions of high magnetic stress, reconnection locally occurs at the X points of a_z [1, 36]. From a qualitative analysis, the size of these current sheets is of the order of few d_i's. The concentration of current in sheetlike structures (Fig. 5-(a)) suggests that also kinetic effects may nuzzle locally as well (note that they also manifest a bifurcation).

To get more insight in this phenomenon, we quantified kinetic effects looking directly at the high-order velocity moments of the DF, concentrating in particular on temperature and the kurtosis of f. The preferred directions of f in the velocity space, for each $\boldsymbol{x}$, can be obtained from the stress tensor

$$A_{i,j}(\boldsymbol{x}) = \frac{1}{n}\int (v_i - \langle v_i\rangle)(v_j - \langle v_j\rangle) f d^3v. \qquad (10)$$

This tensor can be studied in a diagonal form computing its eigenvalues λ_1, λ_2, λ_3 (note that λ_i are the temperatures, choosen for convenience such that $\lambda_1 > \lambda_2 > \lambda_3$, and the respective eigenvectors $\hat{e}_i$ are the anisotropy directions in the minimum variance frame). For a Maxwellian, the tensor in Eq. (10) is diagonal and degenerate. Using the eigensystem, the temperature anisotropy is given by λ_1/λ_3. The PDF of λ_1/λ_3 in Fig. 5-(c) show that f is mostly isotropic, while only few events manifest strong anisotropy ($\lambda_1/\lambda_3 \sim 1.7$). A comparison between the simulations reveals that higher level of turbulence (Runs II and III with $\delta b/B_0$=1/7 while for Run I $\delta b/B_0$=1/3) produces patches with higher anisotropy. The anisotropy, whose shaded contour is represented in Fig. 5-(b), is confined in sheetlike structures (with the size of a few d_i), modulated by the local magnetic field: anisotropy is low inside magnetic islands while is high in between them. The comparison between Fig. 5-(a) with Fig. 5-(b) suggests that these distortions are concentrated in sheetlike regions, located near the peaks of j_z. Therefore these patterns are characterized by intense $|\nabla^2\boldsymbol{b}_\perp|(= |\boldsymbol{\nabla} j_z|)$ - in a fluid model these would

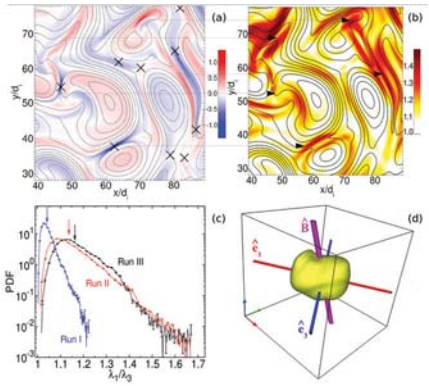

FIGURE 5. (a) Shaded contours (zoom) of j_z together with a_z (isolines) and its X points (black crosses). (b) Shaded contour (same region of panel a) of the anisotropy together with the inplane magnetic field lines (black). (c) PDF of the temperature anisotropy λ_1/λ_3 for all runs (arrows represent averages). (d) Isosurfaces of the velocity DF $f(\boldsymbol{x}^*, \boldsymbol{v})$, at a given spatial position $\boldsymbol{x}^* \simeq (60, 119)d_i$.

correspond to regions where collisional dissipation takes place. The distributions of kurtosis (not shown) manifest strong variations from Maxwellian, suggesting that in turbulence the velocity distributions are leptokurtic. Finally, in Fig. 5-(d) the isosurfaces of f reveal that the DF is strongly affected by the presence of turbulence, resembling a potatolike structure elongated in the $\hat{e}_1$ direction ($\hat{e}_3$ and the direction of the local magnetic field are reported as well).

To summarize, hybrid Vlasov-Maxwell simulations reveal that, in turbulence, kinetic effects manifest as snakelike patches of high anisotropy and kurtosis, the DF results strongly modulated by the turbulent electromagnetic field. This suggests that kinetic effects in plasmas are strongly inhomogeneous, property related to the intermittent character of the magnetic field.

REFERENCES

1. S. Servidio, W. H. Matthaeus, M. A. Shay, P. A. Cassak, and P. Dmitruk, *Phys. Rev. Lett.* **102**, pp. 115003–115003-4 (2009).
2. A. Greco, P. Chuychai, W. H. Matthaeus, S. Servidio, and P. Dmitruk, *Geophys. Res. Lett.*, **35**, L19111–L19114 (2008).
3. A. Greco, W. H. Matthaeus, S. Servidio, P. Chuychai, and P. Dmitruk, *Astrophys. J.*, **691**, pp. L111–L114 (2009).
4. K. T. Osman, W. H. Matthaeus, A. Greco, and S. Servidio, *Astrophys. J.*, **727**, pp. L11–L15 (2011).
5. S. Servidio, F. Valentini, F. Califano, and P. Veltri, *Phys. Rev. Lett.*, **108**, pp. 045001–045001-4 (2012).
6. T. N. Parashar, S. Servidio, B. Breech, M. A. Shay, and W. H. Matthaeus, *Phys. Plasmas*, **17**, pp. 102304–102304-5 (2010).
7. B. U. O. Sonnerup, *J. Plasma Phys.*, **4**, pp. 161–174 (1970).
8. V. M. Vasyliunas, *Rev. Geophys. Space Phys.*, **13**, pp. 303–336 (1975).
9. E. N. Parker, Astrophys. J., **264**, pp. 642–647 (1983).
10. R. Bruno, and V. Carbone, *Living Rev. Solar Phys.*, **2**, lrsp-2005-4.
11. S. Servidio, W. H. Matthaeus, M. A. Shay, P. Dmitruk, P. A. Cassak and M. Wan, *Phys. Plasmas* **17**, pp. 032315–032315-17 (2010).
12. W. H. Matthaeus and S. L. Lamkin, *Phys. Fluids*, **29**, pp. 2513–2534 (1986). (1986)
13. B. U. O. Sonnerup, in *Solar System Plasma Physics*, edited. by E. N. Parker, C. F. Kennel and L. J. Lanzerotti, North-Holland (1979) pp. 47–102
14. K. V. Roberts, and J. B. Taylor, *Phys. Rev. Lett.* **3**, pp. 197–198 (1962).
15. S. Galtier, and E. Buchlin, *Astrophys. J.* **656**, pp. 560–566 (2007).
16. W. H. Matthaeus, S. Servidio, and P. Dmitruk, *Phys. Rev. Lett.*, **101**, pp. 149501–149501-1 (2008).
17. P. Dmitruk, and W. H. Matthaeus, *Phys. Plasmas* **13**, pp. 042307–042307-8 (2006).
18. S. Donato, S. Servidio, P. Dmitruk, V. Carbone, M. A. Shay, P. A. Cassak, and W. H. Matthaeus, *Phys. Plasmas*, **19**, pp. 092307–092307-1 (2012).
19. D. Sundkvist, A. Retino, A. Vaivads, and S. D. Bale, *Phys. Rev. Lett.*, **99**, pp. 025004–025004-4 (2007).
20. L. F. Burlaga, *Solar Phys.*, **4**, pp. 67–92 (1968).
21. M. Neugebauer, *J. Geophys. Res.*, **111**, pp. A04103 (2006).
22. P. D. Mininni, and A. Pouquet, *Phys. Rev. E*, **80**, pp. 025401–025401-4 (2009).
23. E. Marsch, *Living Rev. Solar Phys.*, **3** (2006).
24. K. T. Osman, W. H. Matthaeus, A. Greco, and S. Servidio, *Astrophys. J. Lett.*, **727**, L11–L15 (2011).
25. J. Egedal, W. Fox, N. Katz, M. Porkolab, M. ØOieroset, R. P. Lin, W. Daughton, and J. F. Drake, *J. Geophys. Res.*, **113**, pp. A12207 (2008).
26. D. Biskamp, *Cambridge U. Press*, Cambridge, England (1993).
27. W. H. Matthaeus, and D. Montgomery, *Ann. N.Y. Acad. Sci.*, **357**, pp. 203–222 (1980).
28. S. Ghosh, M. Hossain, and W. H. Matthaeus, *Comput. Phys. Commun.*, **74**, pp. 18–40 (1993).
29. S. Servidio, P. Dmitruk, A. Greco, M. Wan, S. Donato, P. A. Cassak, M. A. Shay, V. Carbone, and W. H. Matthaeus, *Nonlin. Proc. Geophys.*, **18**, pp. 675–695 (2011).
30. P. A. Cassak, and M. A. Shay, *Phys. Plasmas*, **14**, pp. 102114–102114-11 (2007).
31. S. Servidio, V. Carbone, L. Primavera, P. Veltri, P., and K. Stasiewicz, *Planet. Space Sci.*, **55**, pp. 2239–2243 (2007).
32. M. A. Shay, J. F. Drake, R. E. Denton, and D. Biskamp, *J. Geophys. Res.*, **103**, pp. 9165–9176 (1998).
33. S. Servidio, A. Greco, W. H. Matthaeus, K. T. Osman, and P. Dmitruk , *J. Geophys. Res.*, **116**, pp. A09102 (2011).
34. F. Valentini, P. Travnicek, F. Califano, P. Hellinger, and A. Mangeney, *J. Comput. Phys.*, **225**, pp. 753–770 (2007)
35. F. Valentini, F. Califano, and P. Veltri, *Phys. Rev. Lett.*, **104**, pp. 205002–202002-4 (2010).
36. J. F. Drake, M. Opher, M. Swisdak, J. N.Chamoun, *Astrophys. J.*, **709**, pp. 963–974 (2010).